

Electronic structure of the calcium monohydroxide radical

Caroline M. Taylor^{a)}

James Franck Institute and Department of Chemistry, The University of Chicago, Chicago, Illinois 606372

Rajat K. Chaudhuri

Indian Institute of Astrophysics, Bangalore-560034, India

Karl F. Freed

James Franck Institute and Department of Chemistry, The University of Chicago, Chicago, Illinois 60637

(Received 7 September 2004; accepted 25 October 2004; published online 11 January 2005)

Effective valence shell Hamiltonian \mathcal{H}^v calculations are used to map out three-dimensional potential energy surfaces for the 12 lowest electronic states of the CaOH radical. Excitation energies and spectroscopic constants are compared with experiment and prior computations where available, but many previously unavailable data are provided, including excited state dipole moments and oscillator strengths. Particular attention is paid to clarify the nature of nonlinear and quasilinear excited states, Renner-Teller couplings, and state mixings. The $\tilde{F}^2\Pi$ and $\tilde{G}^2\Pi$ ($6^2A'$ and $8^2A'$) states are both found to possess nonlinear local minima, due to an avoided crossing. Attention is also focused on the characteristics of basis sets necessary in high-accuracy calculations for the CaOH radical. © 2005 American Institute of Physics. [DOI: 10.1063/1.1834511]

I. INTRODUCTION

The alkaline earth metal hydroxides are a class of radical salts which have been extensively investigated.^{1–11} From the initial studies of the colors they produce in flames,¹² focus has shifted towards understanding the origin of their underlying electronic structure, and several review articles have appeared.^{13,14} Analysis of this series of molecules has revealed some interesting commonalities.

A small barrier to linearity is found from calculations for the BeOH ground state,¹⁵ while MgOH is quasilinear in its ground state and is bent in the \tilde{A} state.^{16,17} The SrOH and BaOH radicals are linear in their ground states and appear to have bent minima in their excited states.^{18,19} Hence, the bending potential for the ground state progresses from a double well, through flat (quasilinear), to harmonic (linear) over the series. In addition, the existence of a bent excited state tends to appear at increasing energy (generally occurring in the second $^2\Pi$ state) when moving to heavier members of the series. Thus, CaOH occupies an important transitional position in the middle of the series where the physics is ambiguous, and understanding of its underlying structure sheds light on the entire series.

Laser induced fluorescence experiments on CaOH by Pereira and Levy reveal the presence of a high-lying excited state ($\tilde{F}^2\Pi$) which appears to be bent and whose spectrum resists classification.¹ This is surprising as extensive study of the ground state ($\tilde{X}^2\Sigma^+$) of CaOH (Refs. 8, 20–24) shows that it is linear, with bond lengths of $R_{\text{CaO}}=3.731a_0$ and $R_{\text{OH}}=1.807a_0$. Experiments by Li and Coxon on the first excited state ($\tilde{A}^2\Pi$) of CaOH find a slightly smaller Ca–O

distance than in the ground state ($R_{\text{CaO}}=3.691a_0, R_{\text{OH}}=1.809a_0$), and Pereira and Levy report the Ca–O distance for the $\tilde{D}^2\Sigma^+$ state as $R_{\text{CaO}}=3.579a_0$, confirming that the Ca–O distance decreases with excitation for the states with known bond distances. Very little is known experimentally about the $\tilde{B}^2\Sigma^+$ state, but the Ca–O stretching frequency in the $\tilde{E}^2\Sigma^+$ state is slightly higher than in the other states. Studies of the $\tilde{G}^2\Pi$ state find a smaller bending frequency (311 cm^{-1}),³ implying that, like the $\tilde{F}^2\Pi$ state, it possesses some bent character. These observations are consistent with the trends observed in the other alkaline earth metal hydroxides and confirm that unraveling the CaOH electronic structure is germane to understanding the series as a whole.

That the CaOH radical is a linear, ionic molecule in its ground state is intuitively obvious, but this does not explain the presence of substantial complexity in its excitation spectrum. For CaOH to have a bent excited state geometry as proposed, the nature of the bonding must have changed to become more covalent. In fact, the ground state dipole moment is only 1.4 D,²⁵ on the small side for an ionic molecule, which suggests appreciable covalent character is already present. Ligand field calculations for CaOH, SrOH, and BaOH give very poor estimates of the Ca–O distance while dealing well with the other two molecules,⁶ further supporting speculation that CaOH has much lower ionic character. There are, moreover, factors other than charge transfer which may contribute to the observed electronic structure. Among these are symmetry breaking due to Renner-Teller coupling between the nuclear and electronic motions, which may induce deviations from linearity, and surface crossing due to the closeness of low-lying electronic states. The resulting structure of CaOH is undoubtedly due to a combination of these effects.

Available calculations for the lower states of CaOH are

^{a)}Present address: Department of Chemistry and Chemical Biology, Baker Laboratory, Cornell University, Ithaca, New York 14853. Electronic mail: cmtaylor@kffl.uchicago.edu

substantially in agreement with experiment,^{2,7,11,26,27} but only minimal work has appeared for the higher states which exhibit the interesting onset of bent geometries and the capacity for Renner-Teller coupling. Anharmonic constants have been reported only for the ground state, but recent calculations for CaOH using the multireference doubles configuration interaction (MR-DCI) method²⁸ find only a very small barrier to linearity for the $\tilde{F}^2\Pi$ state (~ 50 cm⁻¹, as for BeOH) and a broad, flat bending potential for that state at larger Ca–O distances. These MR-DCI calculations, however, generate weak estimates for the bond lengths and are not of sufficient accuracy to completely resolve the spectral complexity, as they neglect, among other things, core electron correlation which is important in computing accurate geometries for calcium-containing molecules. We address these issues in the present work.

Section II briefly reviews background information concerning the \mathcal{H}^v method, while the computational details are presented in Sec. III. Calculations of three-dimensional potential energy surfaces are described in Sec. IV for the ground state and several excited states (seven for the linear case, 11 for bent geometries). Comparisons with experiment and with other calculations are made where possible, and many results for excited states are reported here. This computation of several three-dimensional surfaces supports the earlier contention^{29,30} that the \mathcal{H}^v method is suitable for studies of global excited state potential energy surfaces, something previously the sole purview of multireference configuration interaction (MRCI) methods.

II. THEORY

As a description of the effective valence shell Hamiltonian method \mathcal{H}^v is presented in detail elsewhere,^{31–33} only a brief overview is provided here.

The effective valence shell Hamiltonian is derived by partitioning the full molecular Hamiltonian \mathcal{H} of the Schrödinger equation in n -electron space into (i) the “primary” space of determinants that have fully occupied core orbitals and empty excited orbitals, with the valence electrons distributed in all possible ways throughout the valence orbitals, and (ii) the “secondary” space of determinants that have at least one core hole and/or occupied excited orbital. The effective valence shell Hamiltonian \mathcal{H}^v is then given by

$$\mathcal{H}^v = \mathbf{P}\mathcal{H}\mathbf{P} + \mathbf{P}\mathcal{H}\mathbf{Q}(\mathcal{E}\mathbf{Q} - \mathbf{Q}\mathcal{H}\mathbf{Q})^{-1}\mathbf{Q}\mathcal{H}\mathbf{P}, \quad (1)$$

where $\mathbf{P} = \sum_p |p\rangle\langle p|$ is the projection operator onto the primary space and $\mathbf{Q} = 1 - \mathbf{P} = \sum_q |q\rangle\langle q|$ is the projector onto the orthogonal complement secondary space.³⁴

While the effective Hamiltonian \mathcal{H}^v acts only on the valence (\mathbf{P}) space, it generates the same eigenvalues \mathcal{E} as does the full Hamiltonian, $\mathcal{H}^v(\mathbf{P}|\psi\rangle) = \mathcal{E}(\mathbf{P}|\psi\rangle)$. Since this equation is not directly soluble, \mathcal{H}^v is treated by expanding the denominator $(\mathcal{E}\mathbf{Q} - \mathbf{Q}\mathcal{H}\mathbf{Q})^{-1}$ and applying quasidegenerate perturbation theory. The Hamiltonian is decomposed into a zeroth-order term and a perturbation, $\mathcal{H} = H^0 + \mathcal{V}$, where $\mathcal{V} \equiv \mathcal{H} - H^0$, and the series is expanded in powers of \mathcal{V} , producing

$$\begin{aligned} \mathcal{H}^v = & \mathbf{P}\mathcal{H}\mathbf{P} + \frac{1}{2} \left(\sum_p \mathbf{P}\mathcal{V}\mathbf{Q}(E_p^0 - \mathcal{H}_q^0)^{-1}\mathbf{Q}\mathcal{V}|p\rangle\langle p| + \text{H.c.} \right) \\ & + \frac{1}{2} \left(\sum_{p,p'} |p'\rangle\langle p'| \mathcal{V}\mathbf{Q}(E_p^0 - \mathcal{H}_q^0)^{-1}\mathbf{Q}\mathcal{V}\mathbf{Q}(E_{p'}^0 - \mathcal{H}_q^0)^{-1}\mathbf{Q}\mathcal{V}|p\rangle\langle p| + \text{H.c.} \right) \\ & - \frac{1}{2} \left(\sum_p \mathbf{P}\mathcal{V}\mathbf{Q}(E_p^0 - \mathcal{H}_q^0)^{-1}\mathbf{Q}(E_p^0 - \mathcal{H}_q^0)^{-1}\mathbf{Q}\mathcal{V}\mathbf{P}|p\rangle\langle p| + \text{H.c.} \right) \\ & + O(\mathcal{V}^{n>3}) \end{aligned} \quad (2)$$

through third order (H.c. denotes the Hermitian conjugate of the preceding term in brackets). In operator notation, \mathcal{H}^v is the sum of the fully correlated core energy \mathcal{E}_c and the correlated one-, two-, three-, and four-electron operators that are present through third order in the \mathcal{H}^v expansion. These effective operators have nonzero matrix elements only between functions containing valence orbitals, and all effects of the core and excited orbitals are included through the perturbation expansion.

The zeroth-order Hamiltonian is a sum of one-electron operators

$$\mathcal{H}^0 = \sum_c \varepsilon_c a_c^\dagger a_c + \varepsilon_{\bar{v}} \sum_v a_v^\dagger a_v + \sum_e \varepsilon_e a_e^\dagger a_e, \quad (3)$$

where a_i and a_i^\dagger are the annihilation and creation operators for the corresponding orbital set; ε_c and ε_e are the (core and excited) orbital energies; and for treating systems with large valence spaces, $\varepsilon_{\bar{v}}$ is the average energy of the valence orbitals. This averaging of the valence orbital energies satisfies the requirements for quasidegenerate perturbation theory and facilitates convergence of the perturbation expansion by avoiding singularities due to small energy differences in the denominators. While the perturbation series may eventually diverge, this happens at high orders (10–100),³⁵ and the third-order estimate is quite accurate. For example, the vertical excitation energies, which provide the most facile comparator, typically approach the true value asymptotically.

TABLE I. Basis sets used for CaOH.

Set	Atomic orbitals (basis functions)
3-21G augmented bI : (14s12p7d2f/7s7p3d2f):126 (88A',38A'') (59A1,9A2,29B1,29B2)	Ca: (12s9p/5s4p) + (2s3p7d2f/2s3p3d2f) O: [(PVTZ:12s7p2d1f/4s3p2d1f)] + (2s2p1d/2s2p1d) H: (Werner:7s2p/5s2p)
Aldrich-Ortiz bI' : (14s12p7d2f/7s7p3d2f):119 (83A',36A'') (56A1,9A2,27B1,27B2)	Ca: (12s9p/5s4p) + (2s3p7d2f/2s3p3d2f) O: (9s3p3d1f/7s3p3d1f) H: (Werner:7s2p/5s2p)
6-311G(2df,2pd) + 3-21G augmented bII : (28s27p12d3f/15s14p6d3f):168 (116A',52A'') (77A1,13A2,39B1,39B2)	Ca: [(14s11p3d/8s7p1d) + (2d1f/2d1f)] + (12s9p/5s4p) + (2s3p7d2f/2s3p3d2f) O: [(11s5p/4s3p) + (2d1f/2d1f)] H: [(5s/3s) + (2p1d/2p1d)]
6-311G(2df,2pd) + 3-21G augmented + g(guess) bII' : (28s27p12d3f1g/15s14p6d3f1g):188 (115A',56A'') (75A1,16A2,40B1,40B2)	Ca: [(14s11p3d/8s7p1d) + (2d1f/2d1f)] + (12s9p/5s4p) + (2s3p7d2f/2s3p3d2f) + (1g(0.89)/1g) O: [(11s5p/4s3p) + (2d1f/2d1f)] H: [(5s/3s) + (2p1d/2p1d)]
6-311G + (3df,3pd) + (fg) + augmented bIII : (16s14p13d4f1g/10s10p6d4f1g):195 (132A',63A'') (87A1,18A2,45B1,45B2)	Ca: [(14s11p3d/8s7p1d) + (3d2f/2d2f)] + (1g(1.05)/1g) + (2s3p7d2f/2s3p3d2f) O: [(11s5p/4s2p) + (3d1f/3d1f) + (diff sp)] H: [(5s/3s) + (3p1d/3p1d) + (diff s)]

This behavior is attributable to the averaging of orbital energies, to the choice of orbitals (see below), and to the inclusion of all diagrams at each order.

The core and ground state occupied valence orbitals are first generated from a self-consistent-field (SCF) calculation for a reference state which may be either the ground state or an excited or ion state. The valence orbitals not occupied in the reference state SCF approximation are generated as improved virtual orbitals (IVOs).³⁶ Finally, dynamical correlation is incorporated by the perturbative corrections in Eq. (2). Both the second- and third-order approximations incorporate contributions from single and double excitations out of the core. An analogous formalism exists to correct the dipole moment operator for contributions from dynamical correlation.³⁷

Because the same set of orbitals is used to describe all of the states, rather than using new orbitals for each as is customary in configuration interaction and other wave function-based methods, a single \mathcal{H}^v calculation describes many states of the system at a given geometry with fairly balanced accuracy at once. The cost of constructing surfaces for all low-lying states described by the valence space is no more than the cost of constructing the surface of a single state. This feature is exemplified by our calculations of three-dimensional potential energy surfaces for CaOH, where, for bent geometries, 12 electronic states are described by a single \mathcal{H}^v calculation.

III. COMPUTATIONAL DETAILS

A. Basis sets

In order to determine the essential ingredients in a basis set for CaOH, potential energy surfaces are constructed using five basis sets as described in Table I. Each basis set is des-

ignated by its calcium contraction set and the total number of basis functions. For example, the first basis set is specified as **bI**: (14s12p7d2f/7s7p3d2f):126, referred to as **bI** for the sake of brevity (see Table I). Also shown in the left column of the table are the numbers of atomic orbitals (basis functions) in each symmetry block.

The first basis **bI** consists of the 3-21G basis of Dobbs and Hehre,³⁸ augmented with two diffuse *s* ($\zeta=0.01, 0.001$) functions, three *p* ($\zeta=0.1522, 0.074\ 979, 0.026\ 927$) functions, three *d* functions (*7d/3d*), and two *f* functions ($\zeta=2.0, 0.3$) to calcium; Dunning's PVTZ correlation consistent basis set,³⁹ augmented with two *s*, two *p* and one *d* functions for oxygen; and Werner and Meyer's (*7s2p/5s2p*) basis set⁴⁰ for hydrogen. The modified first basis, **bI'**, replaces the oxygen set of the first basis with the Coulomb fitting basis of Ahlrichs,⁴¹ which is slightly more deformable. The second basis **bII**, constructed from the 6-311G** basis set^{42,43} for all three atoms augmented with all of the calcium functions from the first basis, is very similar in diffuse and polarization content to **bI**, but increases the number of tight Ca functions. An additional set (**bII'**) with slightly more polarization functions than **bII** is generated from set **bII** simply by adding a set of *g* orbitals ($\zeta=0.89$) to the calcium atom. The fourth set (**bIII**) adds the tight Ca functions from the first set (those added to the 3-21G basis in set **bI**) to the 6-311**G++ set,⁴²⁻⁴⁴ augmented with a set of calcium *g* orbitals [$\zeta=1.05$ (Ref. 45)]. Results of the calculations with all basis sets used are reviewed in the following sections in order to justify the choice of basis set **bII** for detailed analysis of the excited state angular potentials for the $\tilde{F}^2\Pi$ and $\tilde{G}^2\Pi$ states.

The recent work by Koput and Peterson²⁶ refers to an as-yet-unpublished basis set study in which they greatly ex-

TABLE II. Orbitals included in each valence space.

Space	Orbitals
8V	$9\sigma(a_1)4\pi(b_1, b_2)10\sigma(a_1)11\sigma(a_1)1\delta(a_1, a_2)5\pi(b_1)$
10V	$9\sigma(a_1)4\pi(b_1, b_2)10\sigma(a_1)11\sigma(a_1)1\delta(a_1, a_2)12\sigma(a_1)5\pi(b_1, b_2)$
12V	$(10V)6\pi(b_1, b_2)$

pand the available correlation-consistent sets of Dunning³⁹ and claim that an extremely large calcium basis set is needed for accurate calculations for CaOH and related systems. As described in the following sections, we find that a smaller, carefully chosen set yields similar accuracy. The most influential aspect of the basis set appears to be the extent of coverage close to the calcium nucleus, presumably to include adequate core correlation contributions from Ca; inclusion of more diffuse and/or more polarization functions has very little impact. The importance of tight calcium basis functions also stems logically from the almost-cationic nature of the calcium when bonded to the OH group, such that the calcium core electrons are more tightly bound.

B. Symmetry

The linear CaOH molecule is of $C_{\infty v}$ symmetry, so calculations for linear geometries use C_{2v} symmetry (with the molecule along the z axis). Thus the doubly degenerate groups separate or “collapse” into different symmetry blocks (e.g., $\Pi \rightarrow B_1, B_2$). The bent CaOH is of Abelian C_s symmetry (z axis perpendicular to the Ca–O bond), so no collapse occurs for nonzero bend angles. This collapse is a source of potential computational difficulties, as it allows for spurious mixing between orbitals of different symmetry and may result in overall symmetry not being preserved. Use of the IVO-complete active space configuration interaction (IVO-CASCI) routine³⁶ obviates this problem by diagonalizing the Fock operator matrix directly within each symmetry block rather than iterating the eigenvectors. The \mathcal{H}^v computations maintain the full symmetry, and bent state potential energy surfaces correlate smoothly with the linear cases.

C. Valence space

Careful choice of the valence space is critical to the success of balanced simultaneous calculations for multiple excited states. A state can only be well described if the orbitals contributing to the dominant configurations are included in the set of valence orbitals. It is not feasible simply to expand the valence space indefinitely, because the \mathcal{H}^v perturbation series does not converge well at low order if the range of valence orbital energies (before averaging) is excessive or if the energetic separation between the valence and excited orbitals is too small. Additionally, the computational cost increases with the number of valence orbitals (and with the number of electrons in the valence space).

In order to determine the optimum valence space for the CaOH study, calculations are performed with three different spaces which contain 8, 10, or 12 valence orbitals, as described in Table II. The labels in parentheses indicate the orbitals used in C_{2v} . The relevant ground state SCF orbital

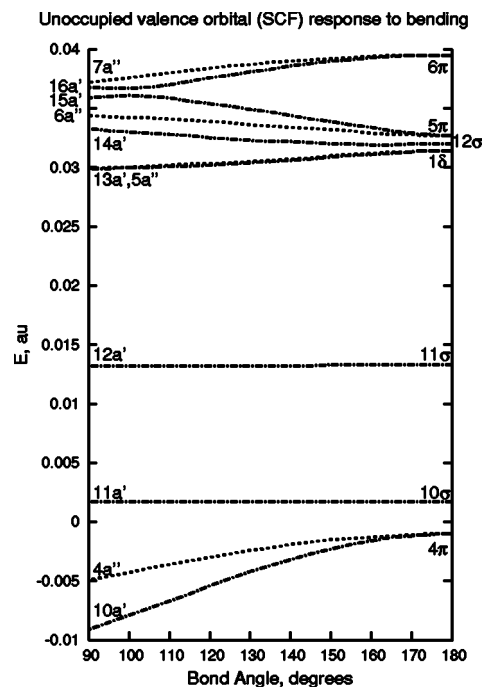


FIG. 1. SCF virtual orbital energies as a function of bending. The left axis corresponds to C_s symmetry and the right to $C_{\infty v}$.

energies are depicted in Fig. 1. The singly occupied HOMO (HOMO—highest-occupied molecular orbital) (9σ) orbital energy is not shown because it lies too low (at -0.082 a.u.). After the IVO calculation, the 9σ orbital is much closer in energy to the other valence orbitals (due to the V^{N-1} IVO potential as opposed to the V^N SCF virtual orbital potential).

The large SCF orbital energy separation (2.2 eV) between the highest occupied molecular orbital (9σ) and the highest core (doubly occupied π) orbital motivates the choice of a valence space with a single active electron. A comfortable energetic separation exists between the 11σ and 1δ orbitals. However, a valence space containing only those orbitals below 1δ cannot describe the higher states (in particular the $\tilde{F}^2\Pi$ state of interest to which the 5π orbital makes the dominant contribution). The next break in the IVO energies falls between the 5π and 6π orbitals. The eight orbital valence space (8V) includes only the b_1 part of the 5π orbital while preserving the full symmetry and does not yield particularly accurate vertical excitation energies for the \tilde{F} state (although other excitation energies are in reasonable agreement with experiment).

The 12σ orbital is omitted from the smallest valence space for the linear geometries, but the energy of the 12σ orbital crosses that of the 5π and 6π orbitals as the Ca–O bond stretches or contracts, and all three orbitals mix extensively for nonlinear geometries. This mixing accounts for the closer agreement with experimental excitation energies for the states with significant population in the higher π orbitals upon the inclusion of the 12σ orbital in the valence space. Consequently, the second valence space, with ten orbitals (10V), augments the 8V space with the 12σ orbital and both the b_1 and b_2 parts of the 5π orbital. Calculations with the 10V space yield a better (i.e., closer to experiment) vertical

TABLE III. Third-order \mathcal{H}^v vertical excitation energies for 8, 10, and 12 valence orbital spaces calculated with basis set **bI**.

State	T_e (eV)			Expt.
	8 V	10 V	12 V	
$\bar{X}^2\Sigma^+$	0.000	0.000	0.000	0.000
$\bar{A}^2\Pi$	2.024	1.986	1.986	1.984 ^a
	2.024	1.986	1.986	
$\bar{B}^2\Sigma^+$	2.205	2.240	2.236	2.234 ^a
$\bar{C}^2\Delta$	2.829	2.884	2.882	2.716 ^a
	2.829	2.884	2.883	
$\bar{D}^2\Sigma^+$	3.537	3.476	3.475	3.490 ^b
$\bar{E}^2\Sigma^+$		3.885	3.881	3.704 ^b
$\bar{F}^2\Pi$	3.919	3.902	3.884	3.746 ^b
		3.902	3.884	
$\bar{G}^2\Pi$			4.092	4.046 ^c
			4.092	

^aReference 24.^bReference 1.^cReference 3.

excitation energy to the $\bar{F}^2\Pi$ state at the ground state experimental geometry, but do not perform well when the molecule bends.

The final, largest valence space, with 12 orbitals (12V), adds the 6π pair to the 10V space. While the vertical excitation energies for the experimental ground state geometry for the 12V space are slightly further from experiment than are those from the 10 valence case, the 12V space performs far better for the bent geometries because it generates essential configurations which contribute to the $\bar{F}^2\Pi$ state, as is illustrated in Sec. IV D.

IV. RESULTS

A. Single point calculations

Table III displays the vertical excitation energies for each valence space, obtained from third-order \mathcal{H}^v calculations at the ground state equilibrium geometry using basis set **bI**. Calculations for linear geometries using both C_{2v} and C_s symmetry confirm that symmetry is conserved. Excitation energies to degenerate states are presented for each orbital in the pair ($\Pi \rightarrow B_1, B_2$ or A', A'') and are identical up the machine limit. The data reflect the ability of the \mathcal{H}^v perturbation series to largely correct for deficiencies in the valence space (provided, of course, that the dominant configurations are included). The excitation energy for the $\bar{F}^2\Pi$ state improves dramatically when the 6π orbital is added to the valence space (10V versus 12V). The energy of the $\bar{C}^2\Delta$ state would likewise improve with expansion of the valence space to include additional δ orbitals.

Table IV summarizes the vertical excitation energies from first-, second-, and third-order \mathcal{H}^v calculations for the 12 orbital valence space with the **bI** and **bII** sets (the other sets behave analogously) at the experimental ground state

equilibrium geometry and using C_{2v} symmetry. Deviations from experiment are in parentheses, and the bottom row gives the average absolute deviations. Coupled cluster singles and doubles (CCSD) calculations using the modified **bI** basis set (**bI'**) have also been performed. In each case, the accuracy from the \mathcal{H}^v calculation is comparable to or better than those found with CCSD. Also included in the table are available experimental and theoretical values for comparison. The gain in accuracy in passing from second to third order is qualitatively independent of the choice of basis set, and a poor initial choice of valence space is compensated for by higher order corrections.

While third order yields an improvement in the accuracy of excitation energies and spectroscopic properties, the second-order \mathcal{H}^v calculations with a reasonable basis set are already as accurate as those found using other methods^{2,7,26,28} (see Table IV), while taking 1/36th as long as third order. Given the accuracy and speed of second-order calculations, the second-order \mathcal{H}^v is a viable method for constructing multidimensional global potential surfaces (which previously could only be accomplished by MRCI), and the full three-dimensional potential surfaces here are constructed only to second order.

The oscillator strengths and dipole moments (Tables V and VI, respectively) are calculated with the **bI'** basis. Although this basis set gives poor spectroscopic properties, it nevertheless yields dipole moments substantially closer to experiment than those from the other sets. This is attributable to the inclusion on oxygen of somewhat more diffuse functions that are more important for dipole moments than for energies. The oscillator strengths consequently also benefit from the extra diffusivity in the **bI'** set. The $\bar{A} \leftarrow \bar{X}$ transition is the strongest of the observed excitations, consistent with the calculated oscillator strength being much larger than the others. At linear geometry, $\Sigma \leftarrow \Delta$ dipole transitions are symmetry forbidden.

The third-order \mathcal{H}^v dipole moment agrees very well with the experimental value for the ground state and the first excited $^2\Sigma^+$ and $^2\Pi$ states. The decrease in dipole moment for the $\bar{A}^2\Pi$ and $\bar{B}^2\Sigma^+$ states indicates that these states are somewhat less ionic than the ground state (and other excited states). The much larger dipole moment calculated for the $\bar{C}^2\Delta$ state is consistent with an increase in its ionic character which we discuss below and which is supported by the similar result found in the ligand field calculation of Allouche.⁶

Calculation of dipole moments for the higher-lying states is problematic. All higher states place the unpaired electron distant from the oxygen nucleus in very diffuse orbitals. The $\langle r^2 \rangle$ values for the \bar{D} through \bar{G} states are $268a_0^2$, $266a_0^2$, $273a_0^2$, and $329a_0^2$, respectively, considerably exceeding the average of $172a_0^2$ for the five lower-lying states, with the difference solely due to the diffuseness of the singly occupied orbital. The dramatic increase in their spatial extent would necessitate the use of even more diffuse functions for accurately calculating the dipole properties of these higher states. Thus, the dipole moments for the \bar{D} through \bar{G} states are not presented. As discussed below, the diffuseness of these states is manifest in other properties also.

TABLE IV. First-, second-, and third-order vertical excitation energies for basis sets **bI** and **bII**, in eV. Parentheses give the absolute deviation from experiment for the \mathcal{H}^v excitation energies.

State	Basis	T_e (eV)			Expt. ^a
		\mathcal{H}_{1st}^v	\mathcal{H}_{2nd}^v	\mathcal{H}_{3rd}^v	
$\tilde{A}^2\Pi$	bI	1.898 (0.09)	2.024 (0.04)	1.986 (0.002)	1.984
	bII	1.902 (-0.08)	2.030 (0.05)	2.012 (0.028)	
	CCSD			1.991	
	Electron propagator ^b			1.880	
	MR-DCI ^c			1.94,1.95	
	Electrostatic polarization ^d			1.981	
	Ligand field ^e			2.51	
$\tilde{B}^2\Sigma^+$	bI	2.323 (0.09)	2.310 (0.07)	2.236 (0.001)	2.234
	bII	2.350 (0.1)	2.358 (0.1)	2.250 (0.02)	
	CCSD			2.229	
	Electron propagator			2.226	
	MR-DCI			2.26	
	Electrostatic polarization			2.214	
	Ligand field			2.61	
$\tilde{C}^2\Delta$	bI	3.056 (0.3)	2.980 (0.3)	2.883 (0.2)	2.716
	bII	3.141 (0.4)	3.013 (0.3)	2.878 (0.2)	
	CCSD			2.862	
	Electron propagator			3.021	
	MR-DCI			3.06,3.05	
	Electrostatic polarization			2.277	
	Ligand field			2.71	
$\tilde{D}^2\Sigma^+$	bI	3.352 (0.1)	3.540 (0.05)	3.475 (0.02)	3.490
	bII	3.346 (-0.1)	3.595 (0.1)	3.552 (0.06)	
	CCSD			3.465	
	Electron propagator			3.285	
	MR-DCI			3.37	
$\tilde{E}^2\Sigma^+$	bI	3.902 (0.2)	3.984 (0.3)	3.881 (0.2)	3.704
	bII	3.956 (0.2)	4.089 (0.4)	3.981 (0.3)	
	CCSD			4.099	
	Electron propagator			3.702	
	MR-DCI			3.74	
$\tilde{F}^2\Pi$	bI	3.832 (0.09)	3.983 (0.2)	3.884 (0.1)	3.746
	bII	3.886 (0.1)	4.082 (0.3)	3.990 (0.2)	
	CCSD			4.095	
	Electron propagator			3.721	
	MR-DCI			3.79,3.80	
$\tilde{G}^2\Pi$	bI	4.003 (0.04)	4.189 (0.13)	4.092 (0.05)	4.046
	bII	4.065 (0.02)	4.302 (0.258)	4.212 (0.2)	
	CCSD			4.193	
	Electron propagator			3.875	
	MR-DCI			3.95,3.96	
$\overline{ dev }$	bI	0.13	0.15	0.075	
	bII	0.154	0.207	0.130	

^aSee notes for Table III.^bReference 2.^cReference 28.^dReference 7.^eReference 6.

B. Analysis of three-dimensional potential energy surfaces

Linear and angular slices of the potential energy surfaces for all 12 of the states are displayed in Figs. 2 and 3, respectively, from second-order calculations with basis set **bII**. Table VII summarizes the computed spectroscopic constants

for these ground and excited state potential surfaces and includes the results from the set closest to experiment if not **bII**.

Although there is evidence of substantial anharmonicity in some excited states, the global minimum for each state occurs at a linear geometry. The excited $^2\Pi$ states have an-

TABLE V. Calculated oscillator strengths for the 12V orbital space with basis **bI'** for CaOH. Results for the 10V space are in parentheses.

Transition	Theory		
	\mathcal{H}_{1st}^v	\mathcal{H}_{2nd}^v	\mathcal{H}_{3rd}^v
$\tilde{X}^2\Sigma^+ \rightarrow \tilde{A}^2\Pi$	0.539 (0.538)	0.573 (0.572)	0.570 (0.567)
$\tilde{X}^2\Sigma^+ \rightarrow \tilde{F}^2\Pi$	0.014 (0.014)	0.018 (0.014)	0.016 (0.015)
$\tilde{X}^2\Sigma^+ \rightarrow \tilde{G}^2\Pi$	0.001	0.00001	0.001

gular potential surfaces which are flat to varying degrees, but those of the lower energy states studied (\tilde{X} through \tilde{E}) exhibit much less bending anharmonicity. In contrast, the $6^2A'$ ($\tilde{F}^2\Pi$) state possesses a nonlinear local minimum, as does the $8^2A'$ ($\tilde{G}^2\Pi$) state (which had not been suspected before this work).

The linear ($C_{\infty v}$) portions of the surface are fit to polynomial functions of order $n=4$ in both distances (R_{CaO} and R_{OH}) to determine the equilibrium bond lengths and harmonic frequencies for the stretching motions.⁴⁶ The calculations for angular geometries (C_s) are treated analogously, but the data are reflected through 0° and fit to polynomials of order $n=6$ in θ^2 . The residuals (higher anharmonicities) for displacements of more than about $0.4a_0$ from equilibrium become substantial, primarily attributable to the decreasing energetic separation between states. This closer spacing allows the configurations to mix extensively, as described below for the \tilde{F} and \tilde{G} states.

1. $\tilde{X}^2\Sigma^+$ ($1^2A'$) state

Basis set **bI** represents the OH group well, but poorly describes the CaO properties, while set **bII** does best for both CaO and OH properties (and the CaOH bend). The O–H separation and stretching frequency from **bII** are closer to experiment than are those found with **bII'**. Since **bII'** contains more polarization functions, this supports the belief that the unpaired electron is polarized away from the metal in the ground state. The expectation that the ground state has little diffuse character is also borne out by the fact that the **bII** set (with fewer diffuse functions than the others) performs best overall for the ground state.

2. $\tilde{A}^2\Pi$ ($2^2A', 1^2A''$) state

The bond lengths and stretching frequencies both agree well with experiment for all the basis sets, and the bending frequency predicted by **bII** is excellent. Set **bIII** gives slightly better values for the OH group, but is equivalent to **bII** for the others. As with the ground state, basis set **bII** yields the best agreement with experiment, implying as above that this state is likewise neither diffuse nor strongly polarized. The linear potential surface is noticeably anharmonic in the Ca–O coordinate, changing little from the ground state, as apparent from the upper middle panel in Fig. 2. The angular potential curves exhibit some Renner-Teller splitting between the $2^2A'$ and $1^2A''$ states (the $1^2A''$ state remains more harmonic).

3. $\tilde{B}^2\Sigma^+$ ($3^2A'$) state

We are not aware of any experimental spectroscopic constants for the \tilde{B} state. The linear potential surface for the \tilde{B} state is slightly more harmonic along the O–H stretching coordinate than in the ground state, which is evident in the upper right-hand plot of Fig. 2, but the calculated frequencies are comparable to those of the ground state, suggesting that the character of the states is similar.

4. $\tilde{C}^2\Delta$ ($4^2A', 2^2A''$) state

The linear potential energy surface of the $\tilde{C}^2\Delta$ state is much shallower and broader along the Ca–O coordinate than are the other states, as illustrated by Fig. 2. The calculated properties in Table VII show the O–H stretching frequency essentially unchanged from the ground state, but the Ca–O stretch is weaker. The much lower Ca–O stretching frequency observed experimentally is consistent with the shape of the calculated potential energy surface. The change in the Ca–O stretch correlates with a much longer Ca–O separation in the $\tilde{C}^2\Delta$ state, suggesting a somewhat greater polarization of the unpaired electron away from the OH group.

5. $\tilde{D}^2\Sigma^+$ ($5^2A'$) state

The calculated spectroscopic properties for the $\tilde{D}^2\Sigma^+$ state are in excellent agreement with experiment for most of the basis sets. Calculations with set **bIII**, with its large num-

TABLE VI. CaOH dipole moments, in D, as calculated with basis **bI'** with 12 valence orbitals at optimized geometries, compared with experiment and other theory.

State	\mathcal{H}_{1st}^v	\mathcal{H}_{2nd}^v	\mathcal{H}_{3rd}^v	Expt. ^a	Other theory		
					LF ^b	EP ^c	CISD ^d
$\tilde{X}^2\Sigma^+$	0.784	1.448	1.539	1.465	1.465/0.8	1.2	0.98
$\tilde{A}^2\Pi$	0.656	0.757	0.801	0.801	1.6/0.9	0.4	0.49
$\tilde{B}^2\Sigma^+$	0.744	0.118	0.573	0.744	2.2/1.5	–0.6	0.11
$\tilde{C}^2\Delta$	5.626	5.690	5.781		5.9/5.1	6.0	
$\tilde{D}^2\Sigma^+$	2.403	–2.832	–1.166				

^aReference 25.

^bLigand field, using experimental/fitted parameters, Ref. 6.

^cElectrostatic polarization, Ref. 7.

^dReference 50.

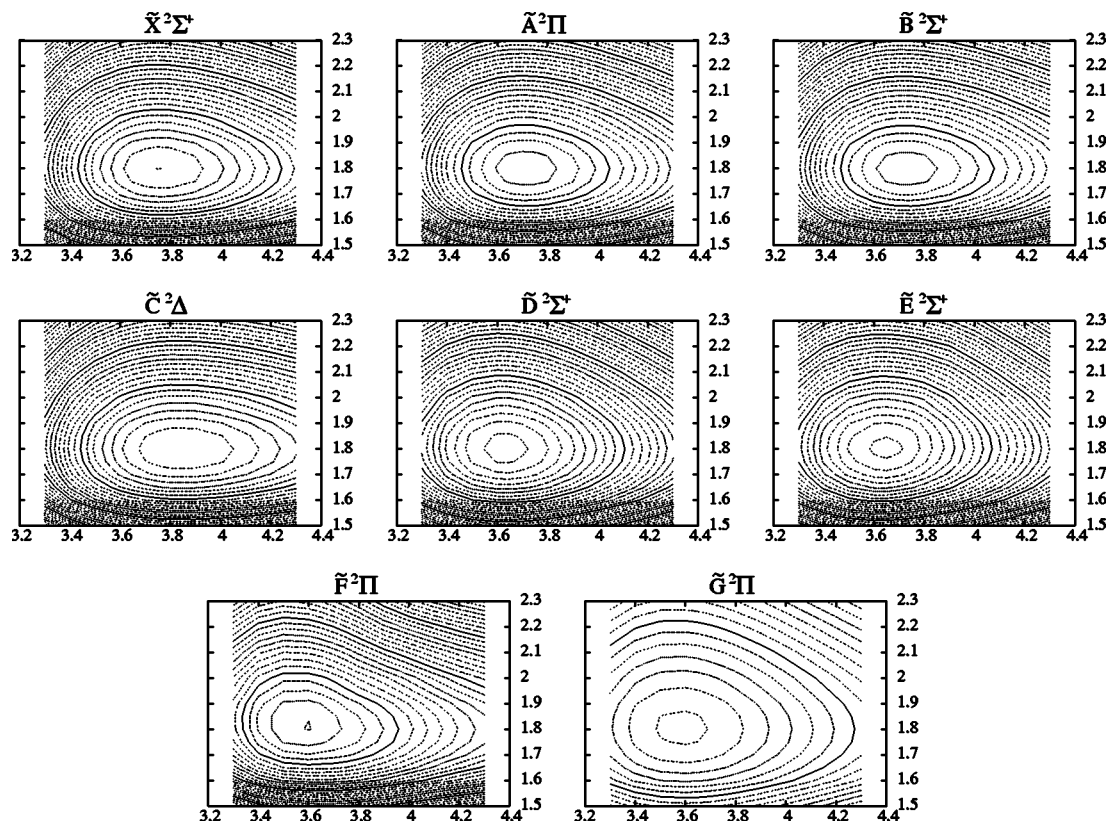


FIG. 2. Linear potential energy surfaces for the ground and excited states of CaOH. Contours are of constant energy, Ca–O separation is on the x axis, O–H on the y axis; all are in atomic units.

ber of polarization and diffuse functions, provide the best agreement. This implies that the \tilde{D} state is quite polarized, and possibly slightly diffuse. The minimum in the linear geometry potential surface shifts to a substantially smaller Ca–O separation from that of the ground state, as visible from the center middle panel of Fig. 2.

6. $\tilde{E}^2\Sigma^+$ ($7^2A'$) state

The geometry changes dramatically upon excitation from the ground state, with the $\tilde{E}^2\Sigma^+$ state minimum occurring at a much shorter Ca–O distance and a substantially larger O–H separation than in the lower states. These changes are clearly visible in the surface (Fig. 2, middle right). The $\tilde{E}^2\Sigma^+$ state is the first to involve non-negligible structural change of the OH group, resulting in a lower O–H stretching frequency and higher Ca–O stretching frequency than for the other states, consistent with experiment. Mixing extensively with the \tilde{F} and \tilde{G} states (discussed in Sec. IV D), the \tilde{E} state also displays a much narrower angular profile (see Fig. 3). Basis set **bII** calculations agree best with experiment, indicating that although the geometry of the state differs from the ground state, the \tilde{E} state is still predominately valencelike, and the tighter calcium functions are necessary for its description.

7. $\tilde{F}^2\Pi$ ($6^2A', 3^2A''$) state

The structure and character of the \tilde{F} state differs drastically from that of the ground state, shifting to a smaller Ca–O separation. A slice along the linear surface at the equilibrium ground (and \tilde{F}) state separation $R_{OH} = 1.8a_0$ (see Fig. 2) displays a very slight shoulder along the Ca–O coordinate, the origin of which is discussed in detail in Sec. IV D. The state splits upon bending, and while both components of the pair have global minima at linear geometries, the $6^2A'$ state changes much more dramatically than the $3^2A''$ (Fig. 3, bottom left panel), developing a *local* nonlinear minimum in its angular potential surface at a 170° bond angle 376 cm^{-1} above the global (linear) minimum; the barrier to linearity is 105 cm^{-1} .

8. $\tilde{G}^2\Pi$ ($8^2A', 4^2A''$) state

Like the \tilde{F} state, the equilibrium geometry of the \tilde{G} state shifts to a smaller Ca–O separation and narrows along the Ca–O coordinate (Fig. 2, bottom right panel). It, too, possesses a local minimum at a nonlinear geometry (in the $8^2A'$ state) which is not visible in the figure: a low barrier to linearity ($\sim 50\text{ cm}^{-1}$) appears 524 cm^{-1} above the global minimum, at a much longer Ca–O distance ($3.841a_0$) than in the $6^2A'$ (\tilde{F}) state, and at a smaller bond angle (158°). Additionally, the angular potential surface of the $8^2A'$ state remains quasilinear over a broader range, corresponding to

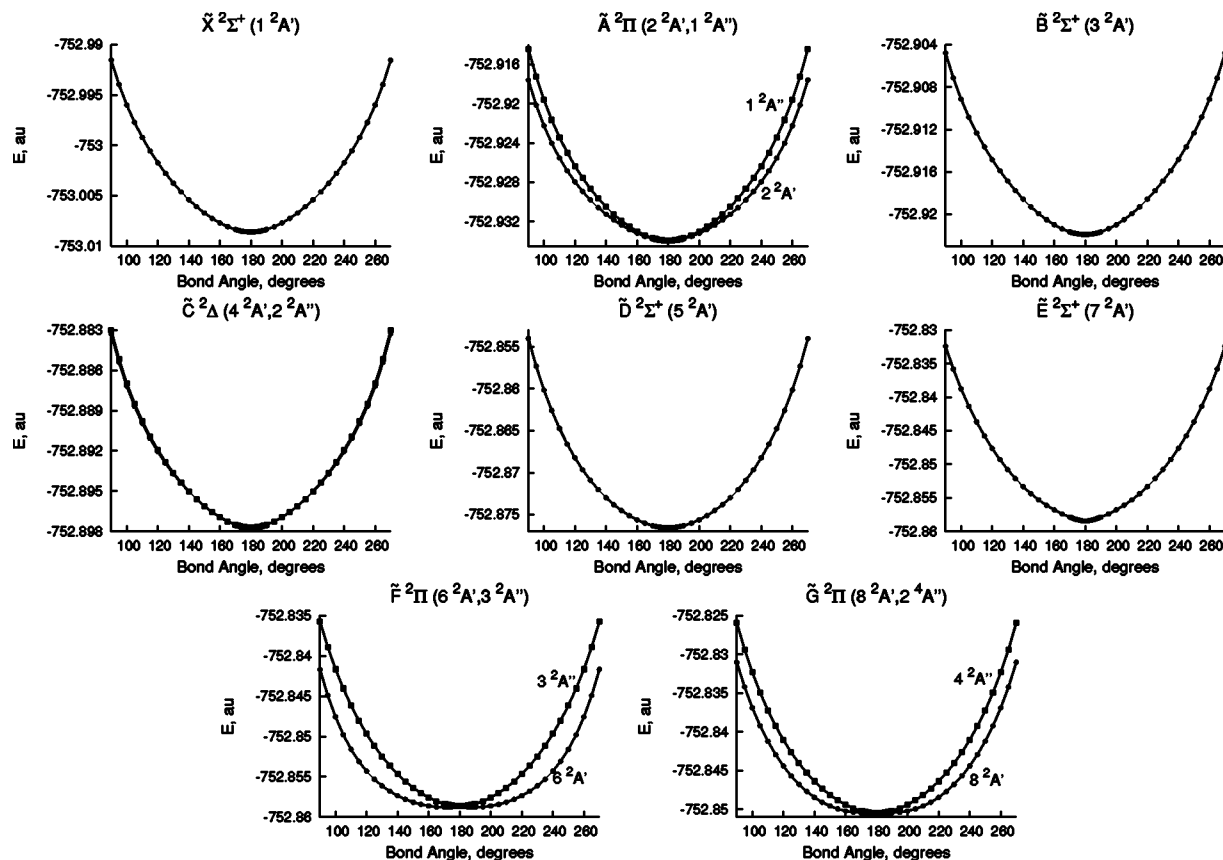


FIG. 3. Angular potential energy surface slices for the ground and excited states of CaOH at $R_{\text{CaO}} = 3.73a_0$ and $R_{\text{OH}} = 1.8a_0$.

this later barrier onset. The large ratio between the fit coefficients of θ^4 and θ^2 (4:1) is characteristic of a quasilinear surface (a very broad, flat angular potential), and since the mode can clearly not be approximated as harmonic, there is poor agreement between the calculated harmonic and experimental frequencies.

C. Spectroscopic properties

Agreement of the \mathcal{H}^v calculated spectroscopic properties with experiment is generally quite good. The Ca–O and O–H stretching frequencies are all within about 6% of the experimental frequencies. The energy of the Ca–O stretch increases for the higher states, except for the $\tilde{C}^2\Delta$ state, which is consistent with experiment. We also observe an overall decrease in the equilibrium Ca–O separation with excitation (again excepting $\tilde{C}^2\Delta$), while the O–H separation changes very little. This is consistent with the hydroxyl group remaining largely unchanged and an experimentally observed O–H stretching frequency very nearly that of OH^- .⁴⁷ However, the harmonic frequencies for the $\tilde{F}^2\Pi$ and $\tilde{G}^2\Pi$ states are not accurate (deviating by about 100 cm^{-1} , $\sim 25\%$, for $\tilde{G}^2\Pi$) because of the very anharmonic shape of their bending potentials.

The valence space employed by these calculations contains five configurations of $^2\Sigma^+$ symmetry, but only a single configuration of $^2\Delta$ symmetry. This is irrelevant for the nonlinear (C_s) portions of the surfaces, as the bent molecule configurations fall into only two symmetry blocks, and thus

there are eight or four ($^2A'$ or $^2A''$, respectively) configurations in the same symmetry block which may mix. This accounts for the close agreement with experiment of the $^2\Sigma^+$ states' excitation energies and properties, while the $^2\Delta$ state transition energy does not match as well (see Table III). A valence space with extra $^2\Delta$ configurations could be used to correct this and to improve the bending frequency of the $4^2A''$ state.

With one exception, other than excitation energies only ground state properties are available from other theories. Theodorakopoulos and co-workers have reported MR-DCI calculations on the first 17 states of CaOH.²⁸ The bond lengths from that work are compared with \mathcal{H}^v calculations and experiment in Table VII. For all three instances in which experimental data are available ($\tilde{X}^2\Sigma^+$, $\tilde{A}^2\Pi$, and $\tilde{D}^2\Sigma^+$), the MR-DCI Ca–O distances deviate by two or three times the deviations of the \mathcal{H}^v second-order calculation, in addition to failing to preserve symmetry. The ground state has been more fully characterized, and the available theoretical and experimental data are summarized in Table VIII. Electron propagator calculations and MR-DCI treatments yield a geometry that deviates substantially from experiment,² while the density functional calculations of Chan and Hamilton¹¹ and CISD work by Bauschlicher *et al.*⁴⁸ both exhibit comparable agreement with experimental bond lengths and Ca–O stretching frequency to that of the second-order \mathcal{H}^v method. Recently reported spin-restricted coupled-cluster [RCCSD(T)] calculations with extremely large basis sets²⁶ yield very good Ca–O and O–H distances and excellent fre-

TABLE VII. Calculated spectroscopic properties for the ground and excited states of CaOH. Distances in atomic units and frequencies in cm^{-1} . Percent deviation from experiment is given in parentheses, where available, and for states other than Σ states, the angular frequencies given are for individual A'/A'' states.

State	Basis set	R_{CaO}	R_{OH}	ω_{CaO}	ω_{OH}	ω_{CaOH}
$\bar{X}^2\Sigma^+$	bI	3.662 52(−1.8)	1.808 18(0.07)	658.1(7.0)	3907.2(3.4)	486.2(36.0)
	bII	3.758 34(0.7)	1.800 56(−0.4)	595.9(−3.0)	3983.3(5.4)	380.8(6.3)
	Expt. ^a	3.731 45	1.806 96	614.8	3778.0	357.2
	MR-DCI ^b	3.83	1.80			
$\bar{A}^2\Pi$	bII	3.707 25(0.4)	1.800 22(−0.5)	622.2(−1.0)	3989.5(6.7)	349.7(−4.5)/389.8(6.4)
	bIII	3.744 02(1.4)	1.802 86(−0.3)	583.2(−7.2)	3966.4(6.1)	402.5(9.8)/435.5(18.0)
	Expt. ^c	3.691 01	1.808 84	628.4	3738.0	366.4
	MR-DCI	3.76	1.80			
$\bar{B}^2\Sigma^+$	bII	3.722 65	1.799 16	602.6	3992.6	381.5
	MR-DCI	3.77	1.80			
$\bar{C}^2\Delta$	bII	3.841 12	1.799 55	505.9(−4.3)	3983.2	289.6(7.2)/287.3(7.9)
	Expt. ^e			528.4		312.2
	MR-DCI	3.83	1.80			
$\bar{D}^2\Sigma^+$	bII	3.648 32(1.9)	1.802 87(−0.33)	659.0(−3.2)	3984.4	433.5(1.9)
	bIII	3.641 07(1.7)	1.805 70(−0.17)	661.1(−2.9)	3961.1	428.9(0.8)
	Expt. ^d	3.579 14 ^g	1.808 85 ^g	681.4		425.6
	MR-DCI	3.70	1.80			
$\bar{E}^2\Sigma^+$	bII	3.566 25	1.822 70	713.2(−3.4)	3771.0	503.6
	Expt. ^d			738		
	MR-DCI	3.65	1.82			
$\bar{F}^2\Pi$	bII	3.642 89	1.803 20	649.3	3971.4	323.8/405.9
	MR-DCI	3.70	1.80			
$\bar{G}^2\Pi$	bII	3.574 36	1.805 56	734.7	3958.4	416.9(34.0)/408.2(31.0)
	bIII	3.611 13	1.807 08	708.0	3949.8	387.3(24.0)/445.4(43.0)
	Expt. ^f					311
	MR-DCI	3.68	1.80			

^aReferences 1 and 24.^bReference 28.^cReference 24.^dReference 1.^eReference 4.^fReference 3.^gFound by assuming the O–H distance in the D state is the same as for the A state.

quencies, but at the cost of a substantially larger basis set than employed in the \mathcal{H}^v calculations.

D. Quasilinearity and the “bent” states

The equilibrium geometries for all 12 CaOH states studied here are linear (see Fig. 3). However, there are substantial features in the bent portions of the potential energy surfaces which suggest that the system is more complicated. Close examination of the $6^2A'$ and $8^2A'$ states reveals that the surfaces are not simply harmonic in the angular dimension but have some local minima at nonzero bend angle (i.e., they have appreciable “bent structure”). In both cases these minima correlate with barriers to linearity, but while the $6^2A'$ state’s barrier is present at the ground state equilibrium geometry, the $8^2A'$ surface is merely quasilinear at those bond separations. At larger Ca–O separations, this flat surface develops into a barrier to linearity. The $7^2A'$ angular potential also exhibits a conical shape indicative of interac-

tions with other states. The effects of state mixing are visible in the potential energy surfaces in the immediate vicinity of 180° (Fig. 4).

These behaviors, which mimic those in the other alkaline earth metal hydroxides, are due to the extensive mixing of the $\bar{F}^2\Pi$ and $\bar{G}^2\Pi$ states with the $\bar{E}^2\Sigma^+$ state. Each state configuration is an admixture of determinants of the form (core) v , where v is the occupied excited orbital (5π , 12σ , or 6π). As the molecular geometry changes from linear to bent and the symmetry decreases from $C_{\infty v}$ to C_s , the initially forbidden mixing becomes allowed, and all three states have components which may mix. This state mixing is clearly evident from the weights of each configuration contributing to the states, which are plotted in Fig. 5, and their shapes are characteristic of an avoided crossing.

The character of the $\bar{F}^2\Pi$ ($6^2A'$) state changes dramatically with small deviations from linearity at the ground state equilibrium separation, with π and σ configuration weights varying by nearly a third (Fig. 5, top panel). This very strong

TABLE VIII. Comparison of calculated (\mathcal{H}^v) spectroscopic properties with experiment and various theoretical studies for the $\tilde{X}^2\Sigma^+$ of CaOH. Distances are in bohrs and frequencies in wave numbers.

Method	R_{CaO}	R_{OH}	ω_{CaO}	ω_{OH}	ω_{CaOH}
$\mathcal{H}^v_{2\text{nd}}$	3.758 34	1.800 56	595.9	3983.3	380.8
CISD ^a	3.756 78	1.79	629		
Elec Prop ^b	3.815 36	1.827 37			
DFT ^c	3.755	1.811 5	624	3966	427
MR-DCI ^d	3.83	1.80			
RCCSD(T) ^e	3.737 12	1.799 02	612.1	3873	347.6
Experiment ^f	3.731 45	1.802 04	614.8	3778	357.2

^aReference 48.^bReference 2.^cB3LPY/6-311G+ + **, DZVP, Ref. 11.^dReference 28.^eReferences 1 and 24.^fReference 26.

coupling between the $6^2A'$ and $7^2A'$ states is balanced by a change in the character of the $7^2A'$ state, depicted in the middle panel of Fig. 5, corresponding quite clearly to an avoided crossing between the $6^2A'$ and $7^2A'$ states. MR-DCI calculations for the ground and excited states of CaOH have led to postulation that there is an avoided crossing between these two states,²⁸ which we confirm. This avoided crossing creates the barrier to linearity at the ground state equilibrium geometry and extends along the Ca–O coordinate in the $6^2A'$ ($\tilde{F}^2\Pi$), resulting in a broad and shallow minimum and the complexity observed in the experimental spectra.

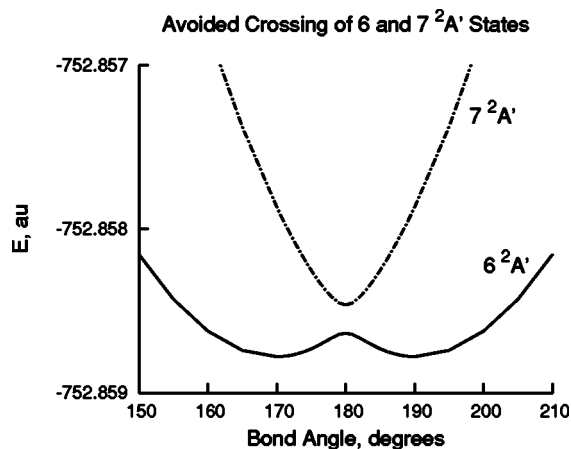
The mixing of the three highest $2A'$ states is also responsible for the quasilinear behavior observed in the $\tilde{G}^2\Pi$ state. Because the coupling between the $7^2A'$ and $8^2A'$ states is much weaker than between $6^2A'$ and $7^2A'$ states (see the lowest plot in Fig. 5) and because they approach each other at larger Ca–O separation, the bending potential of the $8^2A'$ state flattens. The state remains quasilinear over a broader range of geometries than does the $6^2A'$ ($\tilde{F}^2\Pi$) state, and the barrier to linearity develops at geometries further from the ground state equilibrium geometry. The barrier is also correspondingly lower in the $8^2A'$ ($\tilde{G}^2\Pi$) state, only about half of that for the $6^2A'$ ($\tilde{F}^2\Pi$) state, a consequence of the smaller coupling between the configurations. The barrier would likely increase with inclusion of higher states with which the $8^2A'$ state couples.

The computed 0.01 eV spacing between the $\tilde{E}^2\Sigma^+$ and $\tilde{F}^2\Pi$ states at the ground state equilibrium geometry is clearly smaller than the margin of error for any *ab initio* method, and the \tilde{E} and \tilde{F} state order is inverted compared to experiment at this point. At the *experimental* minimum geometry ($R_{\text{CaO}}=3.732a_0$, $R_{\text{OH}}=1.803a_0$), the \tilde{E} state is calculated to lie 0.013 eV above the \tilde{F} state, while at the minimum geometry extracted from the fit to the $\tilde{X}^2\Sigma^+$ surface ($R_{\text{CaO}}=3.758a_0$, $R_{\text{OH}}=1.800a_0$), the \tilde{E} state is only 0.0016 eV above the \tilde{F} state. At $R_{\text{CaO}}=3.758a_0$ and $R_{\text{OH}}=1.803a_0$, it is 0.013 eV *below* the \tilde{F} state. Hence for linear geometries the ordering of the $\tilde{E}^2\Sigma^+$ and $\tilde{F}^2\Pi$ is very sensitive to changes

in the Ca–O coordinate, and they cross at almost exactly the experimental geometry (at $R_{\text{CaO}}=3.7125a_0$ and $R_{\text{OH}}=1.8a_0$). A change in the ordering of the \tilde{E} and \tilde{F} states at the ground state equilibrium geometry is equivalent to shifting the surface for the \tilde{E} state up or down, which merely changes where the crossing occurs, not the fact of its occurrence. This is true as well for the $\tilde{G}^2\Pi$ state, since the location of the barrier to linearity in the $\tilde{G}^2\Pi$ ($8^2A'$) state is dependent upon where the $\tilde{E}^2\Sigma^+$ state crosses it.

V. DISCUSSION

The \mathcal{H}^v calculations provide vertical excitation energies and spectroscopic properties in very good agreement with experiment for the ground and 11 excited states of the CaOH radical. Analysis of several basis sets demonstrates that accurate studies of excited states in calcium-containing systems require the inclusion of many tight functions on the calcium atom, due to the tighter binding of the calcium electrons and the impact of core electron correlation. These features are evident from the improved agreement with experiment of the equilibrium Ca–O separation and stretching frequency for the second basis set **bII**, which adds extra tight orbitals about the calcium atom but does not contain additional polarization

FIG. 4. Avoided crossing of the 6 and $7A'$ states.

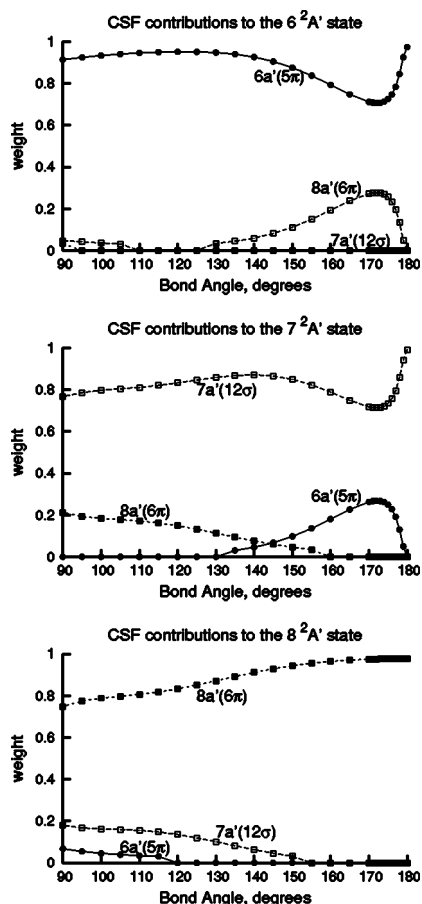


FIG. 5. Configurational mixing among the 6, 7, and 8A' (\tilde{F} , \tilde{E} , and \tilde{G}) states.

or diffuse functions, which are less significant for molecules where calcium is dominantly cationic. The importance of tight functions on Ca apparently applies for the excited states as well as the ground state. The basis set which generates the best molecular (or atomic) spectroscopic properties or geometries is not necessarily optimal for energies,⁴⁹ so the lower quality of the single point properties calculated with set **bII** is not unexpected. Basis set **bI** gives better vertical excitation energies and **bI'** the best dipole moments, but the bond lengths and frequencies calculated with set **bII** are closest to experiment for the majority of the states.

We find that the hydroxide group structure does not change substantially with electronic excitation. Only in the $\tilde{E}^2\Sigma^+$ state is there perceptible alteration of the OH group, with a decreasing Ca–O distance accompanied by an increasing O–H separation. In this state, the polarization of the molecule increases and causes an increase in the dipole moment. The decrease in dipole moment of the $\tilde{A}^2\Pi$ and $\tilde{B}^2\Sigma^+$ states from the ground state value is due to movement of the unpaired electron more toward the calcium atom.

The electronic structure of CaOH fits very well into the larger context of the alkaline earth metal hydroxide series, displaying the anticipated linear ground state and also exhibiting the advent of appreciable structure in the angular dimension higher in its spectrum. While the $\tilde{F}^2\Pi$ state's equilibrium geometry is linear, it quite clearly exhibits a local

bent minimum 376 cm^{-1} above the global minimum at a bond angle of 170° , with a barrier to linearity of 105 cm^{-1} . This feature appears higher in the excitation spectrum than those of both BeOH and MgOH which are found to possess much deeper global minima in the $\tilde{A}^2\Pi$ state (at bond angles of about 115° with barriers of about 2200 and 3700 cm^{-1} , respectively).¹⁵ The subsequent $\tilde{G}^2\Pi$ state of CaOH also has a very flat, quasilinear angular potential at the ground state equilibrium geometry and develops a barrier to linearity at large Ca–O separation. The presence of this barrier in the $\tilde{G}^2\Pi$ is predicted for the first time here, and we expect that similar structure is present in the other alkaline earth metal hydroxides. Because of much weaker coupling with the \tilde{E} state, however, the barrier in the \tilde{G} state is smaller than that in the \tilde{F} state.

The barriers to linearity present in both the $\tilde{F}^2\Pi$ and $\tilde{G}^2\Pi$ states arise from surface crossings with the \tilde{E} state which are allowed in the high-symmetry linear geometry but become avoided by symmetry for any deviation from linear. While the barriers to linearity are low in both the \tilde{F} and $\tilde{G}^2\Pi$ states, the \tilde{F} state's nonlinear well occurs at the ground state equilibrium geometry and is thus readily accessible upon excitation, resulting in the spectral complexity encountered experimentally.

The calculation of global potential energy surfaces for the \tilde{X} through \tilde{G} states of CaOH with the second-order \mathcal{H}^v is highly efficient, costing only as much as constructing a single state surface and yielding the full set of states to comparable accuracy (with the exception of the $\tilde{C}^2\Delta$ state). The method thus allows for cheap, balanced, and efficient surface construction, while still providing energies and spectroscopic properties of the same level of accuracy as other, more costly, methods which require individual calculations for each state's surface. Even greater efficiency will be possible with the implementation of routines for analytic derivatives.

ACKNOWLEDGMENTS

This research was supported, in part, by PRF Grant No. 37939-AC7 and NSF Grant No. CHE-9727655. The authors thank Charles Martin for much helpful discussion.

¹R. Pereiraand and D. H. Levy, J. Chem. Phys. **105**, 9733 (1996).

²J. V. Ortiz, J. Chem. Phys. **92**, 6728 (1990).

³R. A. Hailey, C. Jarman, and P. F. Bernath, J. Chem. Phys. **107**, 669 (1997).

⁴C. N. Jarman and P. F. Bernath, J. Chem. Phys. **97**, 1711 (1992).

⁵Z. Morbi, C. Zhao, J. W. Hepburn, and P. F. Bernath, J. Chem. Phys. **108**, 8891 (1998).

⁶A. R. Allouche and M. Aubert-Frécon, J. Mol. Spectrosc. **163**, 599 (1994).

⁷J. M. Mestdagh and J. P. Visticot, Chem. Phys. **155**, 79 (1991).

⁸M. Li and J. A. Coxon, J. Chem. Phys. **102**, 2663 (1995).

⁹M. Li and J. A. Coxon, J. Chem. Phys. **97**, 8961 (1992).

¹⁰G. M. Greetham and A. M. Ellis, J. Phys. Chem. **113**, 8945 (2000).

¹¹W.-T. Chan and I. P. Hamilton, Chem. Phys. Lett. **297**, 217 (1998).

¹²J. F. W. Herschel, Trans. R. Soc. Edinburg **9**, 445 (1823).

¹³P. F. Bernath, *Spectroscopy and Photochemistry of Polyatomic Alkaline Earth Containing Molecules*, Advances in Photochemistry (Wiley, New York, 1997), see Vol. 23, pp. 1–62.

¹⁴P. F. Bernath, Science **254**, 665 (1991).

¹⁵G. Theodorakopoulos, I. D. Petsalakis, and I. P. Hamilton, J. Chem. Phys. **111**, 10484 (1999).

- ¹⁶A. J. Apponi, M. A. Anderson, and L. M. Ziurys, *J. Chem. Phys.* **111**, 10919 (1999).
- ¹⁷S. K. Jain, C. Rout, and R. C. Rastogi, *Chem. Phys. Lett.* **331**, 547 (2000).
- ¹⁸M. S. Beardah and A. M. Ellis, *J. Phys. Chem.* **110**, 11244 (1999).
- ¹⁹S. J. Pooley, M. S. Beardah, and A. M. Ellis, *J. Electron Spectrosc. Relat. Phenom.* **97**, 77 (1998).
- ²⁰L. M. Ziurys, W. L. Barclay, Jr., and M. A. Anderson, *Astrophys. J. Lett.* **384**, L63 (1992).
- ²¹C. T. Scurlock, D. A. Fletcher, and T. C. Steimle, *J. Mol. Spectrosc.* **159**, 350 (1993).
- ²²D. A. Fletcher, M. A. Anderson, W. L. Barclay, and L. M. Ziurys, *J. Chem. Phys.* **102**, 4334 (1995).
- ²³L. M. Ziurys, D. A. Fletcher, M. A. Anderson, and W. L. Barclay, Jr., *Astrophys. J., Suppl. Ser.* **102**, 425 (1996).
- ²⁴M. Li and J. A. Coxon, *J. Chem. Phys.* **104**, 4961 (1996).
- ²⁵T. C. Steimle, D. A. Fletcher, K. Y. Young, and C. T. Scurlock, *J. Chem. Phys.* **96**, 2556 (1992).
- ²⁶J. Koput and K. A. Peterson, *J. Phys. Chem. A* **106**, 9595 (2002).
- ²⁷J. Kong and R. J. Boyd, *J. Chem. Phys.* **103**, 10070 (1995).
- ²⁸G. Theodorakopoulos, I. D. Petsalakis, H.-O. Liebermann, R. J. Buenker, and J. Koput, *J. Chem. Phys.* **117**, 4810 (2002).
- ²⁹J. E. Stevens, K. F. Freed, M. K. Arendt, and R. L. Graham, *J. Chem. Phys.* **101**, 4832 (1994).
- ³⁰J. E. Stevens, R. K. Chaudhuri, and K. F. Freed, *J. Chem. Phys.* **105**, 8754 (1996).
- ³¹S. Iwata and K. F. Freed, *J. Chem. Phys.* **65**, 1071 (1976).
- ³²M. G. Sheppard and K. F. Freed, *J. Chem. Phys.* **75**, 4507 (1981).
- ³³K. F. Freed and M. G. Sheppard, *J. Phys. Chem.* **86**, 2130 (1982).
- ³⁴S. Iwata and K. F. Freed, *Chem. Phys.* **11**, 433 (1975).
- ³⁵R. K. Chaudhuri and K. F. Freed, *J. Chem. Phys.* **107**, 6699 (1997).
- ³⁶D. M. Potts, C. M. Taylor, R. K. Chaudhuri, and K. F. Freed, *J. Chem. Phys.* **114**, 2592 (2001).
- ³⁷H. Sun and K. F. Freed, *J. Chem. Phys.* **88**, 2659 (1988).
- ³⁸K. D. Dobbs and W. J. Hehre, *J. Comput. Chem.* **7**, 359 (1986).
- ³⁹T. H. Dunning, *J. Chem. Phys.* **90**, 1007 (1989).
- ⁴⁰H. J. Werner and W. Meyer, *J. Chem. Phys.* **74**, 5794 (1981).
- ⁴¹K. Eichkorn, O. Treutler, H. Ohm, M. Haser, and R. Ahlrichs, *Chem. Phys.* **240**, 283 (1995).
- ⁴²R. Krishnan, J. Binkley, R. Seeger, and J. Pople, *J. Chem. Phys.* **72**, 650 (1980).
- ⁴³J.-P. Blaudeau, M. P. McGrath, L. Curtiss, and L. Radom, *J. Chem. Phys.* **107**, 5016 (1997).
- ⁴⁴T. Clark, J. Chandrasekhar, G. W. Spitznagel, and P. Schleyer, *J. Comput. Chem.* **4**, 294 (1983).
- ⁴⁵S. S. Wesolowski, R. A. King, H. F. Schaefer III, and M. A. Duncan, *J. Chem. Phys.* **113**, 701 (2002).
- ⁴⁶G. Herzberg, *Infrared and Raman Spectra of Polyatomic Molecules* (van Nostrand Reinhold, Princeton, NJ, 1954).
- ⁴⁷N. H. Rosenbaum, J. C. Owrtusky, L. M. Tack, and R. J. Saykally, *J. Chem. Phys.* **84**, 5308 (1986).
- ⁴⁸C. W. Bauschlicher, Jr., S. R. Langhoff, and H. Partridge, *J. Chem. Phys.* **84**, 901 (1986).
- ⁴⁹A. Szabo and N. S. Ostlund, *Modern Quantum Chemistry: Introduction to Advanced Electronic Structure Theory*, 1st ed. (McGraw-Hill, New York, 1989).
- ⁵⁰C. W. Bauschlicher, Jr., S. R. Langhoff, T. C. Steimle, and J. E. Shirley, *J. Chem. Phys.* **93**, 4179 (1990).